CHAPTER 4

RESULTS AND DISCUSSION

4.1 Synthesis of colloidal TiO_2 NPs by the sparking process

This section presents the results of colloidal TiO_2 NPs which was successfully prepared by the sparking process. The relationship between weight loss and sparking time, morphology, structural, optical properties and antibacterial activity of the obtained NPs are also discussed.

4.1.1 Relationship between NP concentration and sparking time

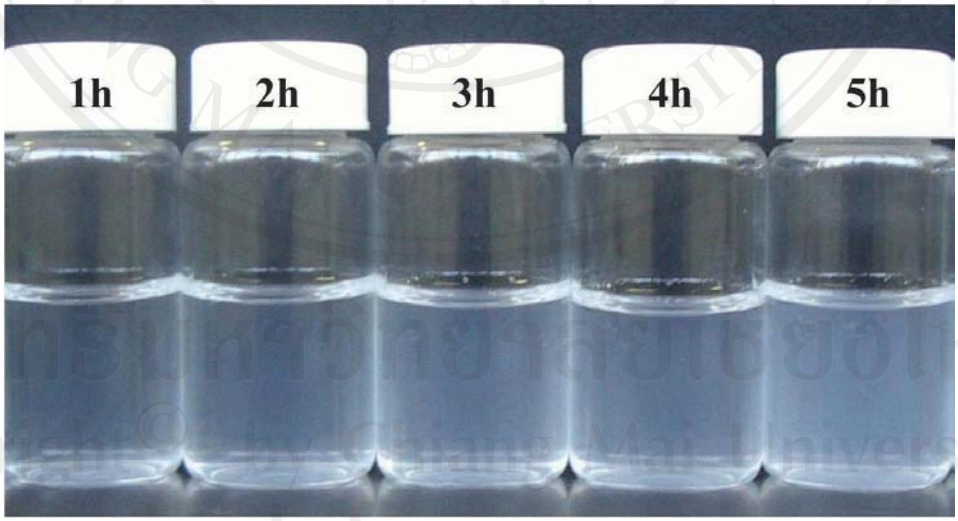

Figure 4.1 Photograph of TiO_2 NPs deposited into 10 mL of distilled water at various sparking time.

Figure 4.1 shows a photograph of colloidal TiO_2 NPs which were prepared by the sparking process for 1 to 5 h in glass bottles filled with 10 mL of distilled water. The NP concentrations of each condition can be determined by the weight loss of Ti wires, as shown in Figure 4.2.

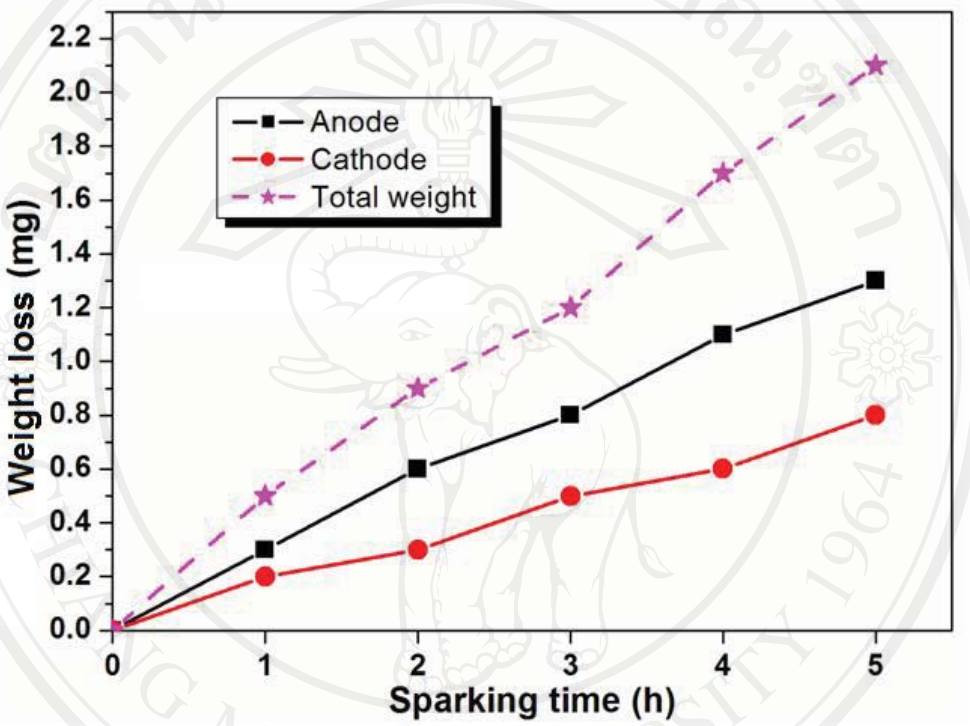

Figure 4.2 Weight loss of Ti wires vs. sparking time.

Figure 4.2 shows the total weight loss of Ti wires increased linearly with increasing the sparking time. However, the weight at anode side has lost more than cathode side due to the bombardment of electrons on Ti tip at anode side shows high kinetic energy (which occurred from the small electron size and high amount of electrons) than the bombardment of ions on Ti tip at cathode side (which occurred from low kinetic energy, high ions size and low amount of ions).

In the case of total mass which were determined by the weight of the obtained NPs after dried each colloidal sample (see Figure 4.1) on aluminum foil have shown in Figure 4.3.

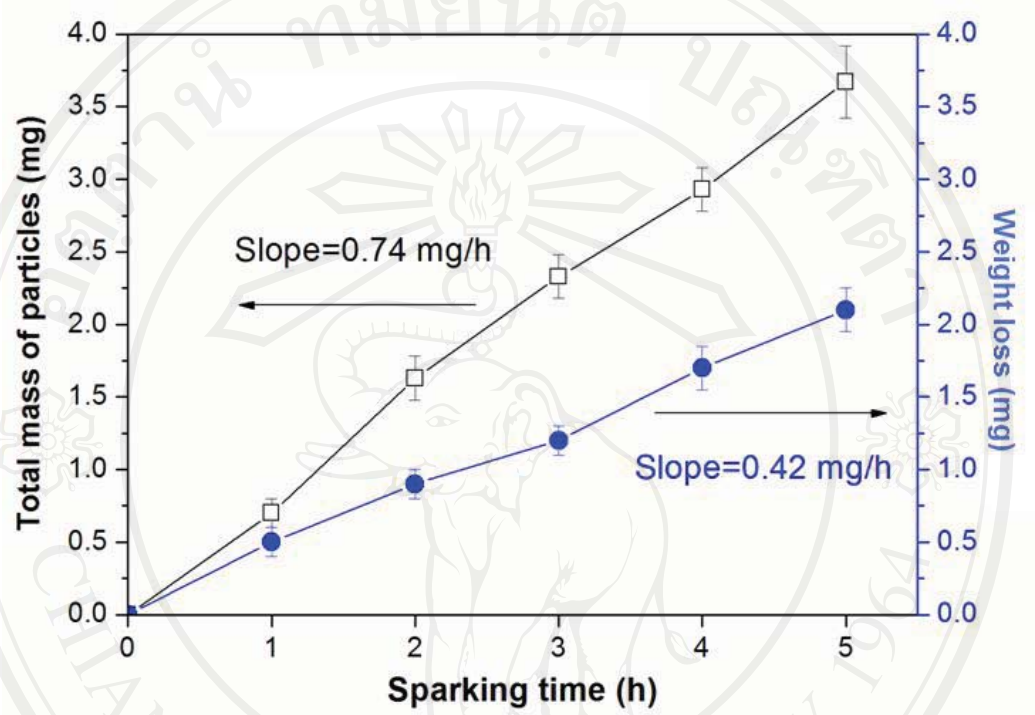

Figure 4.3 Total mass of the NPs and weight loss vs. sparking time.

From the figure, the total weight loss with the rate (slope) of 0.42 mg/h can be converted into mol unit (M), as shown in equation 4.1

$$\text{Total weight loss (M)} = \frac{total\ \ weig\,ht\ loss\ \ (g)}{molecular\ \ \ or\ atomic\ \ weig\,ht\ (\frac{g}{M})} = \frac{0.42\ mg\,/h}{47.87\ g/M} = 8.77\ \mu M \quad (4.1)$$

By assuming that the most of total weight loss of Ti with atomic weight of 47.87 g/M oxidized to form TiO_2 (with the molecular weight of 79.87 g/M), the total TiO_2 can be written as:

$$\text{Total } TiO_2 \text{ (M)} = total\ weight\ loss\ (M) \times \frac{molecular\ \ weig\,ht\ of\ TiO_2\ g/M}{atomic\ \ weig\,ht\ of\ Ti\ g/M}$$

$$= (8.77\ \mu M) \times \frac{79.87\ g/M}{47.87\ g/M}$$

$$= 14.63\ \mu M \qquad (4.2)$$

Whereas the total mass of TiO_2 particles from the figure 4.3 with the rate (slope) of 0.74 mg/h can be converted into M, as shown in equation 4.3

$$\text{Total mass (M)} = \frac{total\ \ mass\ \ (g)}{molecular\ \ weig\,ht\ of\ TiO_2(\frac{g}{M})} = \frac{0.74\ mg/h}{79.87\ g/M} = 9.26\ \mu M \qquad (4.3)$$

Comparison between equation 4.2 and 4.3, the result showed that the total mass of TiO_2 particles from the experiment (4.3) lower than the total TiO_2 from the assuming of weight loss (4.2) due to some TiO_2 lose to the system, such as adhered at the bottle, aluminum foil and Ti wires.

4.1.2 Morphology

The primary particle sizes and their size distributions of as-prepared sample at a sparking time of 1h were in a range of 1-5 nm, as shown in Figure 4.4a and Figure 4.5.

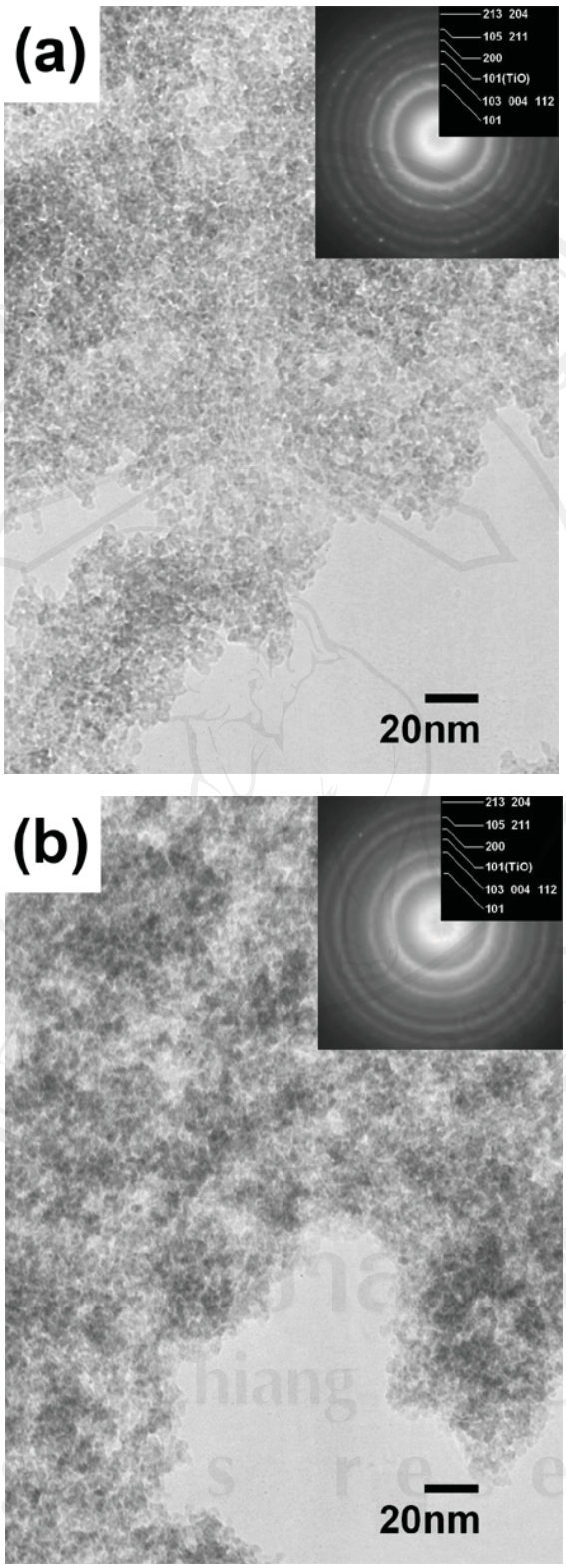

Figure 4.4 TEM images and their corresponding SAED patterns of as-deposited NPs at sparking times of (a) 1 h, and (b) 5 h.

However, at the longer sparking time of 5h (Figure 4.4b), density and agglomeration of the particles increased whereas the primary particle sizes were in the same range. The similar SAED patterns of samples for sparking times of 1 and 5h (Figure 4.4a and 4.4b insets) have shown the five main sharp diffraction rings of (101), (004), (200), (211) and (204) planes which corresponded to the anatase (tetragonal) phase [71].

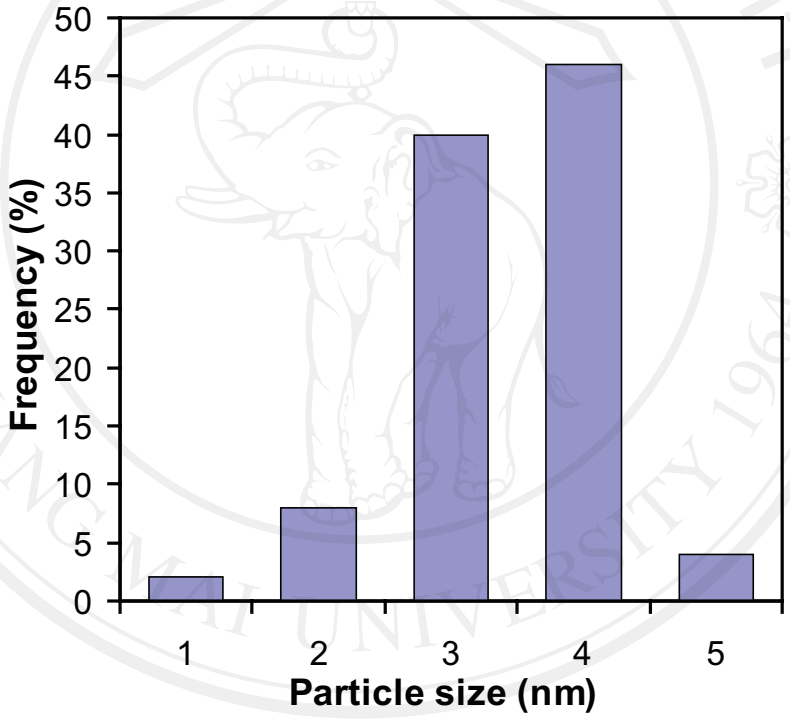

Figure 4.5 Size distributions of the as-prepared TiO_2 NPs

The secondary particle sizes of the as- prepared sample, the annealed samples at 250 and 500 °C were shown in Figure 4.6.

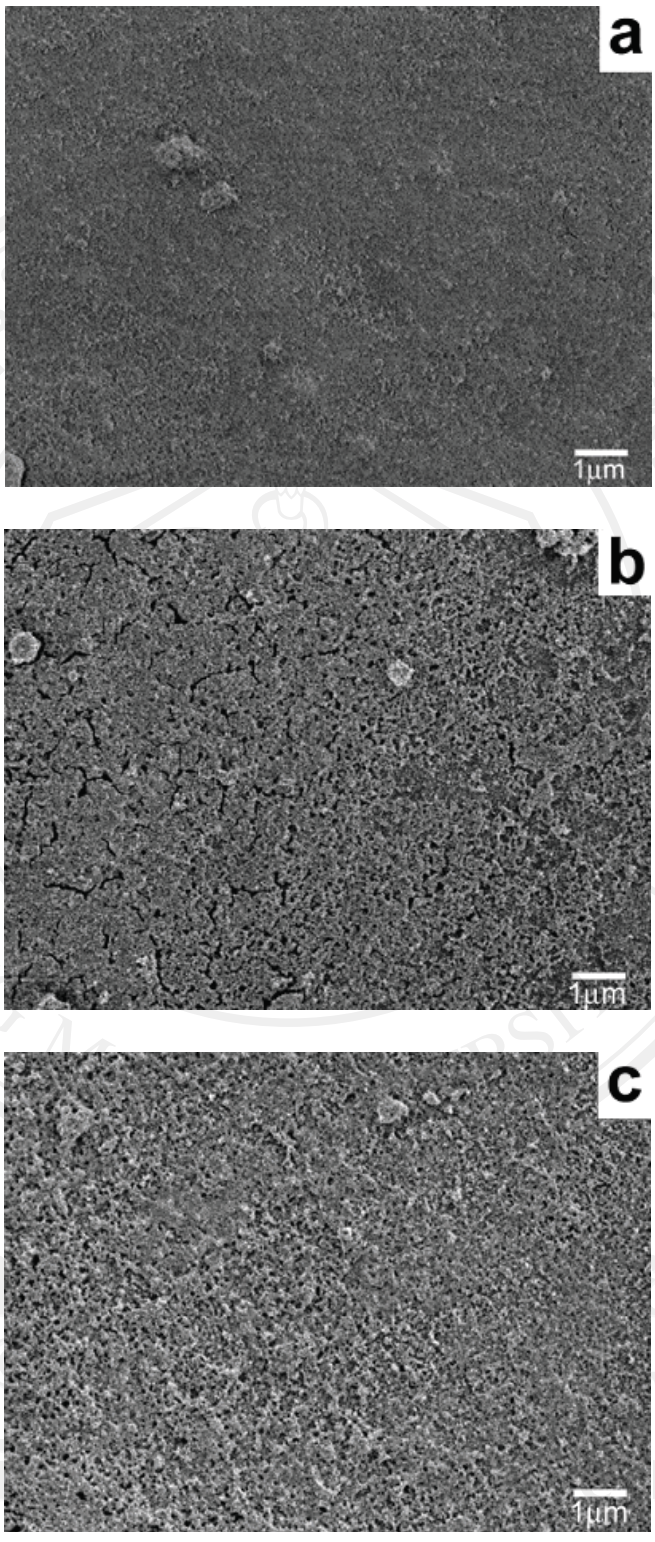

Figure 4.6 SEM images of (a) the as-deposited NPs on quartz substrate by two drops of the NP-dispersed water (b) the annealed sample at 250 and (d) 500°C

SEM images in Figure 4.6a, b and c show the as-prepared TiO_2 NPs deposited on quartz substrates by the two drops of NP-dispersed water and the annealed samples at 250 and 500 °C for 1 h in air, respectively. It is noted that the secondary particle sizes of the samples increased with increasing the annealing temperature [72,73].

4.1.3 Structural properties

Figure 4.7a shows Raman spectra of the as-prepared sample and the annealed samples at 250 and 500 °C. The peaks corresponded to the anatase and rutile phases are marked. It is noted that the anatase peaks at 148, 200, 405, 519 and 638 cm^{-1} increased with increasing annealing temperature. This result is in good agreement with the previous report that different TiO_2 crystalline structures were obtained from different annealing temperatures [74].

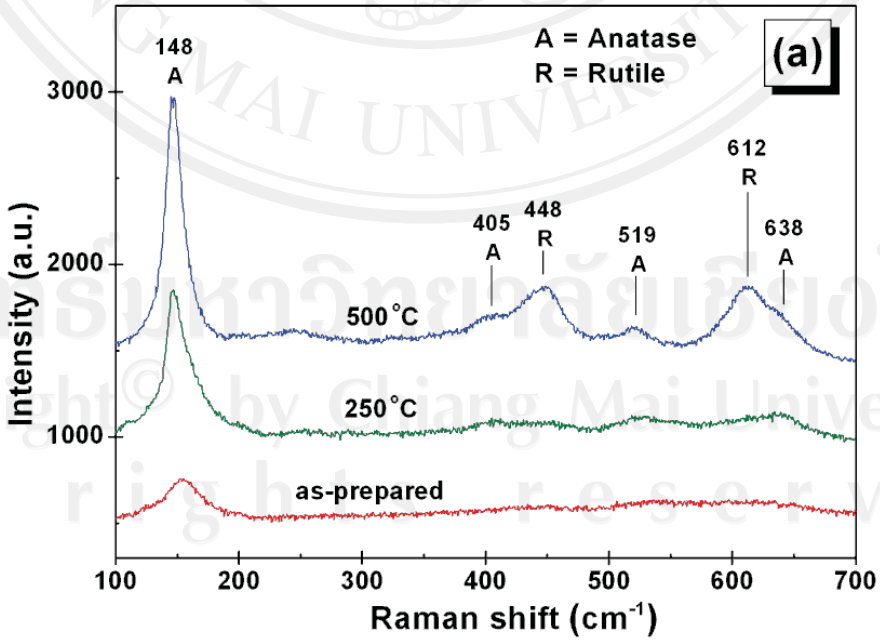

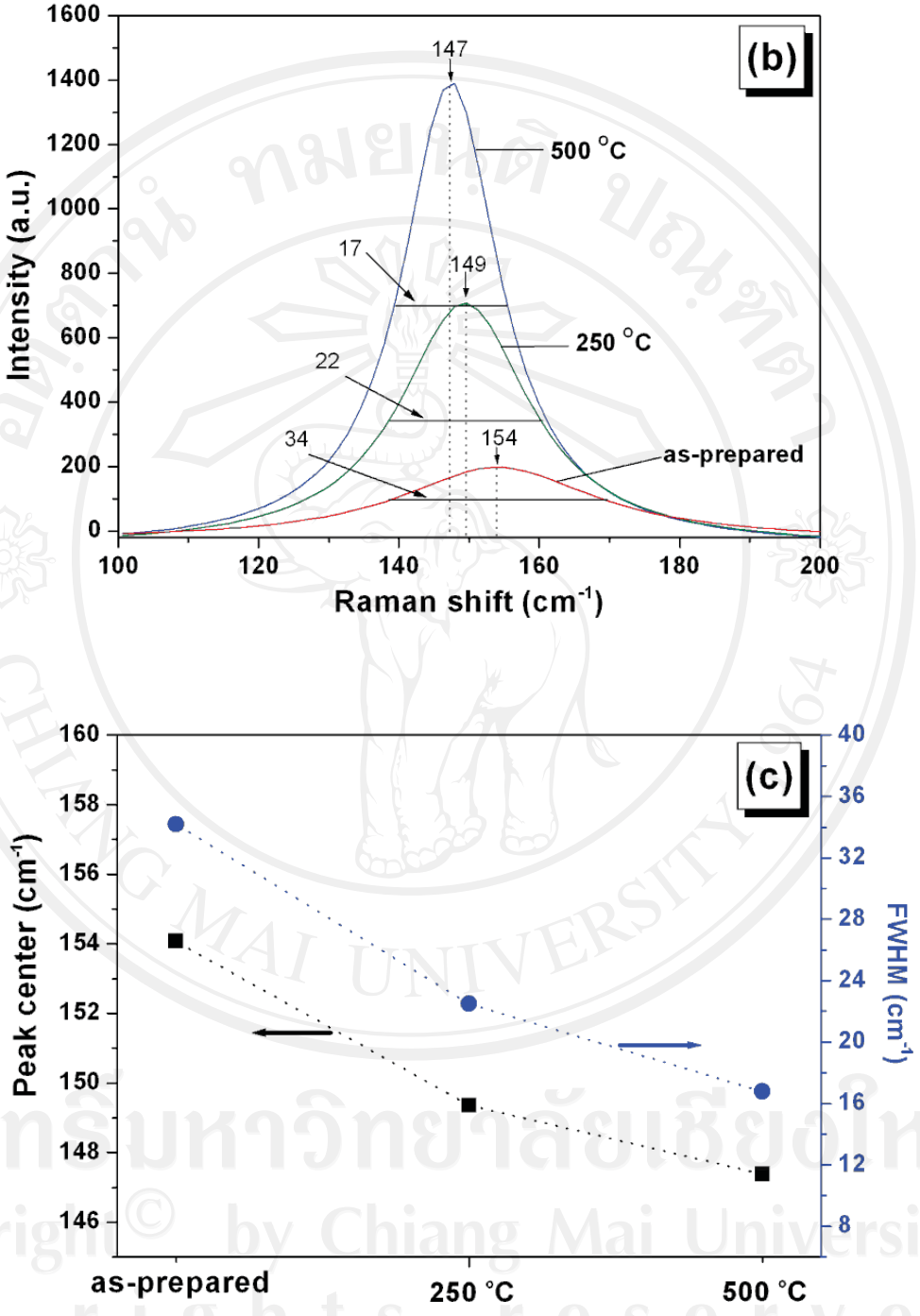

Figure 4.7 (a) Raman spectra, (b) the main anatase peak and (c) plot of main anatase peak and its FWHM against the as-prepared NPs, the annealed samples at 250 and 500 °C.

The annealed sample at 500 °C shows strong anatase peaks at 148 cm^{-1} with the relative anatase/rutile phase ratio of about 80%. However, weak rutile peaks at 448 and 612 cm^{-1} with the relative anatase/rutile phase ratio of about 20% were also observed. Interestingly, the anatase-rutile phase transformation temperature in this work is lower than the reports of Xia and co-workers and Kim and co-workers [75,76]. Xia and co-workers have shown the effect of heat treatment on TiO_2 particle sizes which was prepared by vapor-phase hydrolysis. The results showed the anatase-rutile phase transformation of the samples with 45, 25 and 15 nm in size decreased with decreasing heat treatment from 950 to 750 and 650 °C, respectively. Kim and co-workers have shown nanocrystalline TiO_2 powder which was prepared by solvothermal route from the $Ti(OR)_4$ precursor precipitated in toluene under different concentrations. The results showed the phase transformation temperature increased from 650 to 750 °C with an increase in the particle sizes from 11 to 21 nm. It is attributed that the high specific surface area of the smaller size anatase TiO_2 NPs transformed to the rutile phase at the lower temperature, as compared in Table 4.1 and Figure 4.8.

Table 4.1 Comparison of anatase-rutile phase transformation temperature at various particle sizes of TiO_2 NPs.

Result from	Mean diameter (nm)	Transformation temperature (°C)
This work	3	500
Kim et al. [76]	11	650
	21	750
Xia et al. [75]	17	650
	25	750
	45	950

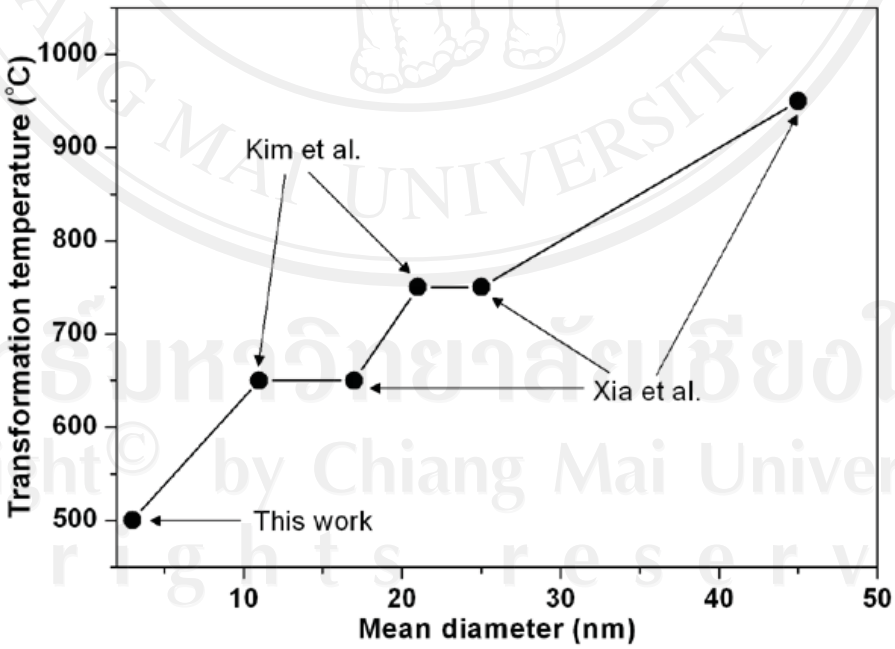

Figure 4.8 Plot of the phase transformation temperature against the mean particle size of TiO_2 NPs.

Figure 4.7b shows a relative intensity, a peak center and a full width at half maximum (FWHM) of the strong anatase peak at approximately 148 cm^{-1}. It is well known that the anatase peaks strongly depend on the annealing temperature [74]. As apparently seen, the weak peak and the stronger peaks were observed from the as-prepared sample and the annealed samples, respectively. Under closer examination, the FWHM change and the peak-center shift are in good agreement with the report of Zhang and co-workers, as shown in Figure 4.7c. These results showed red shift to lower energy due to the increasing and/or agglomeration of the particle to form the bigger sizes which were attributed to phonon confinement and non-stoichiometry effects [77].

4.1.4 Optical properties

The UV–vis transmission spectra of the samples prepared as for Raman spectra are shown in Figure 4.9.

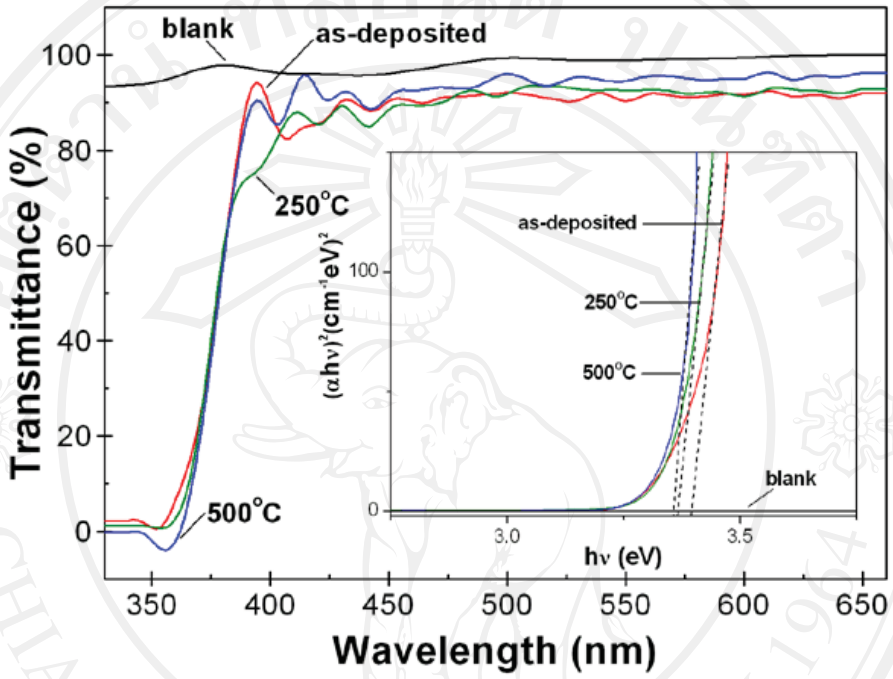

Figure 4.9 Plots of optical transmittance against the wavelength of the as-deposited NPs and the annealed samples at 250 and 500 °C for 1 h. Inset: the variation of $(\alpha hv)^2$ versus hv of the thin films for estimation of the E_g

The light transmittance (T) of approximately 90 % was slightly changed within the wavelength range from 650 to 400 nm and abruptly decreased to less than 5% from 395 to 350 nm. The result has shown that the photon energy absorption fairly corresponds to TiO_2 energy gap [78]. The inset of Fig. 4.9 shows $(\alpha hv)^2$ plotted as a function of the photon energy (hv), where α is the absorption coefficient; $\alpha = ln(1/T)$ [79]. By assuming that the electron transition between the conduction and valence bands was a direct transition, the energy gap was estimated by extrapolating

linearly to $(\alpha h\nu)^2 = 0$ [80]. According to the relative anatase/rutile phase ratio of the annealed sample at 500 °C exhibited 80% of anatase phase which higher than rutile phase (20%; see page 64). Thus, the annealed sample at 500 °C is also used the direct transition. As the result, the energy gaps of the as-prepared sample, the annealed samples at 250 and 500 °C were estimated to be 3.40, 3.36 and 3.35 eV, respectively. The obtained energy gaps were slightly blue-shifted from bulk TiO_2, which were reported to be 3.2 eV for anatase and 3.0 eV for rutile [81]. Such the result was attributed to the phonon confinement effect, crystalline defects and/or oxygen defects [82].

Degradation of MB by colloidal TiO_2 NPs for various sparking times under sunbath for 1 h is shown in Figure 4.10.

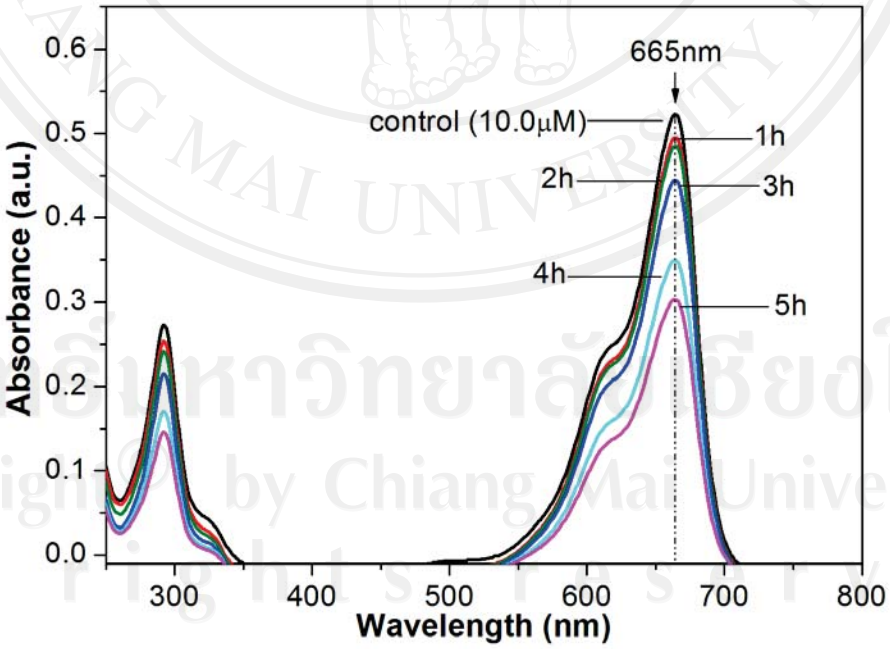

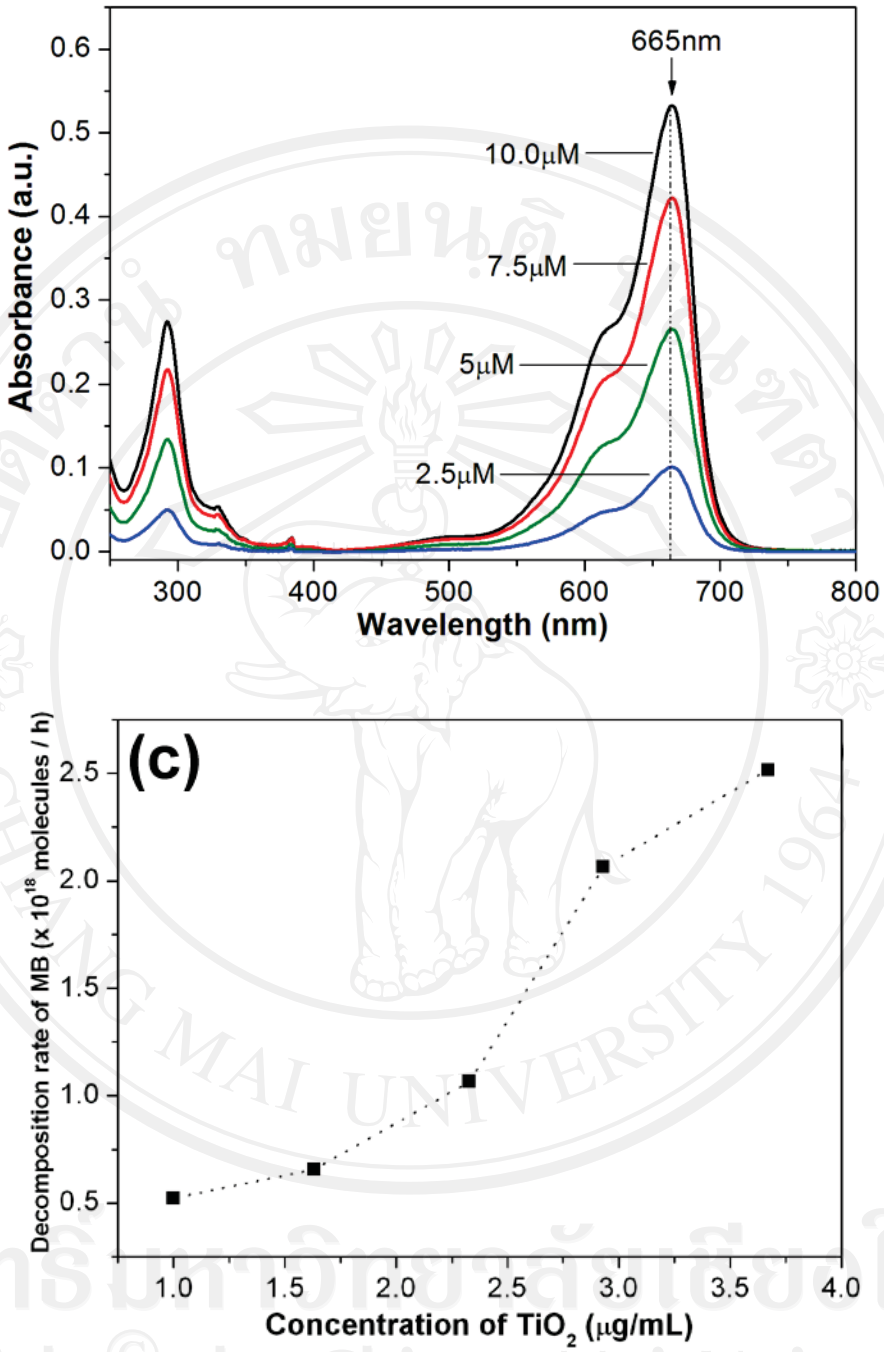

Figure 4.10 Temporal spectral changes of MB solution, (a) concentration of 10 μM containing the as-prepared TiO_2 NPs at the various sparking times under sunbath for 1 h, (b) at dilute concentrations from 10 μM to 2.5 μM without TiO_2 NPs, and (c) decomposition rate of MB vs. concentration of TiO_2 NPs.

As expected, the absorption peaks occurred commonly at 665 and 292 nm [83-85] and the peaks gradually decreased with increasing of the sparking time from 1 to 5 h. In other words, the degradation of MB gradually increased with increasing concentration of the NPs. Moreover, fundamental photocatalytic activity of TiO_2 NPs was investigated by a calibration using UV-vis absorption of dilute MB solution without TiO_2 NPs, as shown in Figure 4.10b, and the obtained mass of TiO_2 NPs, as shown in Fig. 4.3. Decomposition rate of MB at 10 μM were in the range of 0.5 to 2.5×10^{18} molecules/h for the solution containing TiO_2 NPs at dilute concentration of 1.0 to 3.67 μg/mL, as shown in Figure 4.10c.

As shown in the TEM images of Figure 4.4(a and b), the sparking time affects not only the concentration of TiO_2 NPs but also the agglomeration to form bigger secondary particles consequently, reduce photocatalytic activity. However, the used TiO_2 concentration in this work is dilute, therefore the decomposition rate of MB still increased with increasing TiO_2 concentration. The defect of agglomeration is probably high at the higher concentration of TiO_2 NPs.

4.1.5 Anti-bacterial activity

Figure 4.11a, b and c show the growth of *E.coli* which were kept under UV light without the NPs, supplemented with the NPs in the dark and under UV light for various reaction time, respectively.

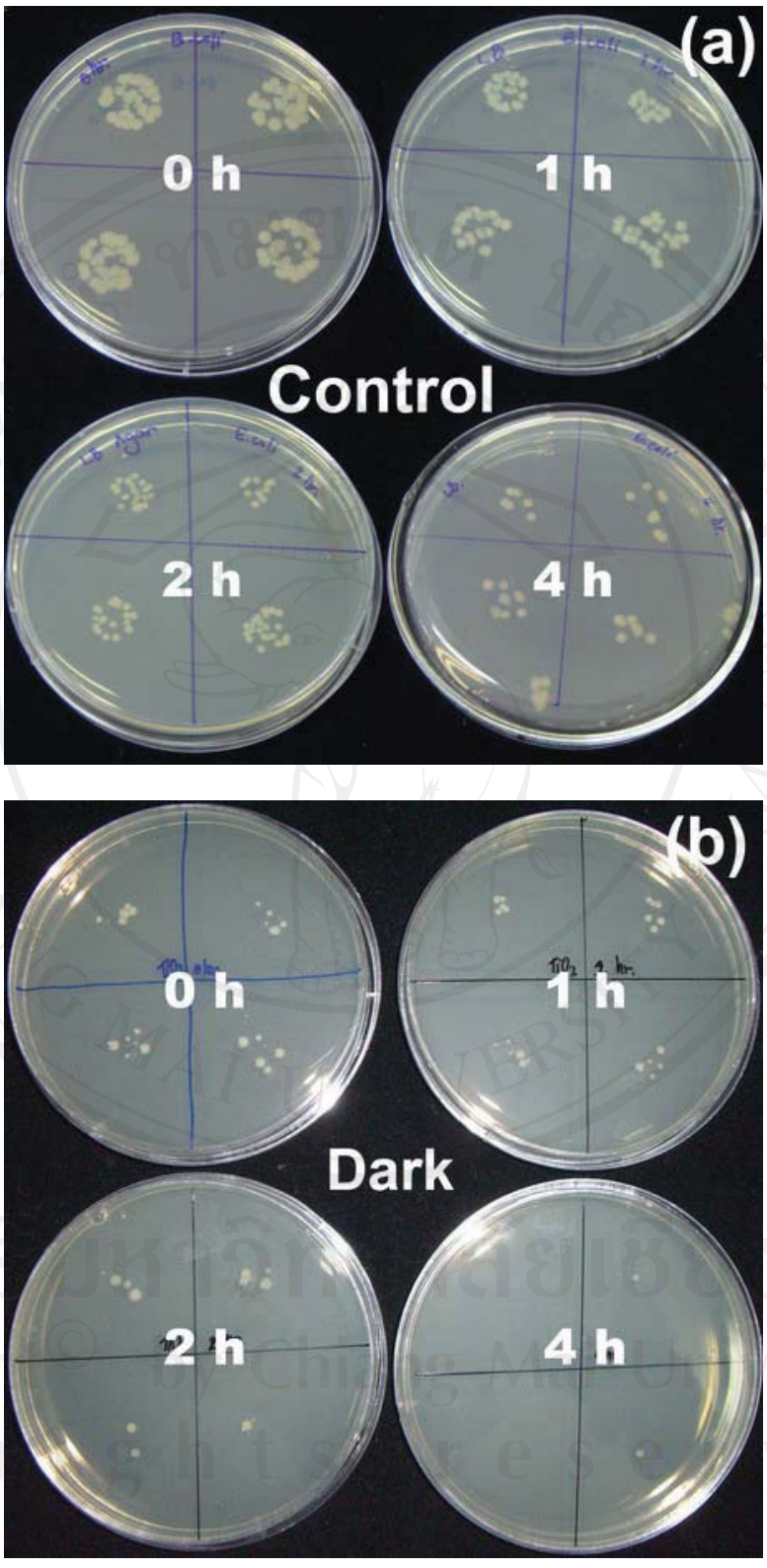

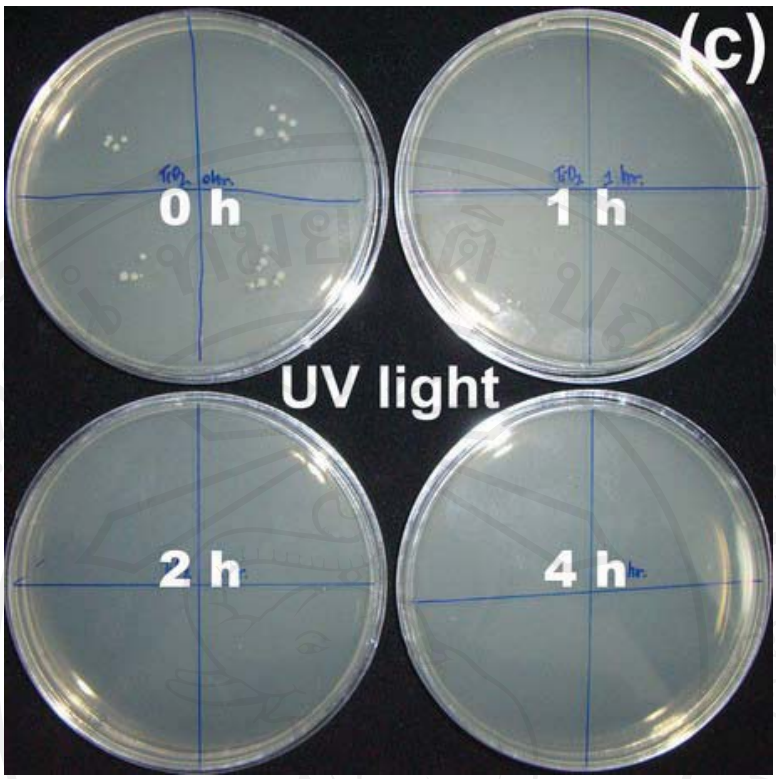

Figure 4.11 Petri dishes of *E.coli* (a) in UV light without TiO_2 NPs and supplemented with TiO_2 NPs (b) in the dark and (c) under UV light, incubated at reaction times of 0, 1, 2 and 4 h

Colonies count was made and plot as a survival rate as showed in Figure 4.12.

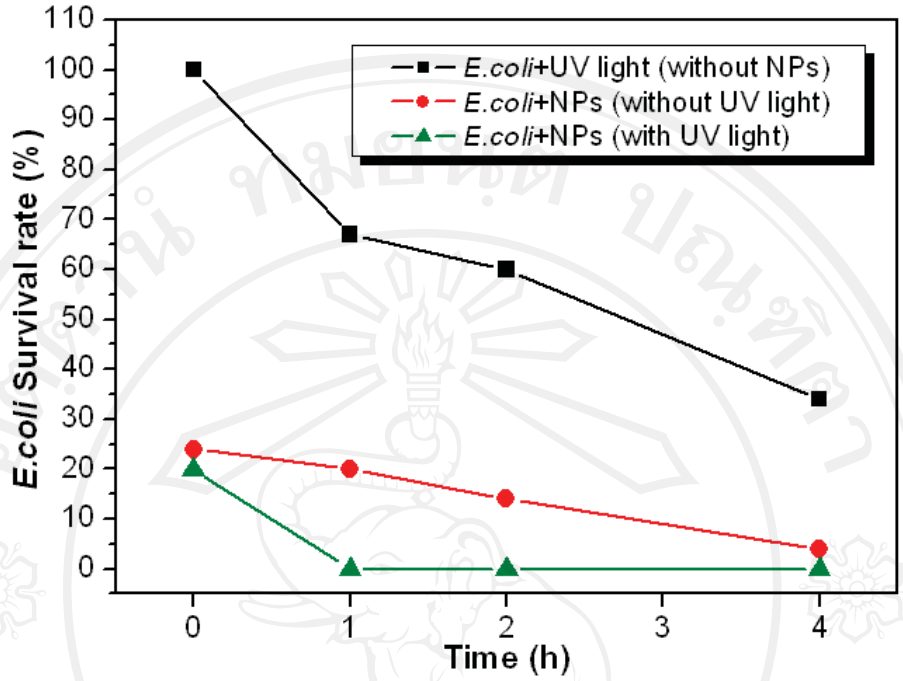

Figure 4.12 Plot of the survival rates of *E.coli* against the reaction time in UV light without NPs, supplement with NPs in the dark and under UV light.

Under the UV light without NPs, the survival rate of *E.coli* decreased from 100 % to 67, 60 and 34 % at the reaction time of 0, 1, 2 and 4 h, respectively. While the survival rate of *E.coli* treated with NPs in the dark highly decreased from 24 to 20, 14 and 4 %. Interestingly, the survival rate of *E.coli* with NPs under UV light abruptly decreased from 20 to almost 0 % within 1 h. This result is in good agreement with some previous works that the UV light itself can be used to treat the *E.coli* [86-90]. It is clearly seen that the antibacterial effect of the NPs themselves is better than that of the UV light whereas that of both factors together is the best.

Figure 4.13 shows SEM images of the morphologies of *E.coli* cells before (a) and after treated with NPs under UV light for 4 h.

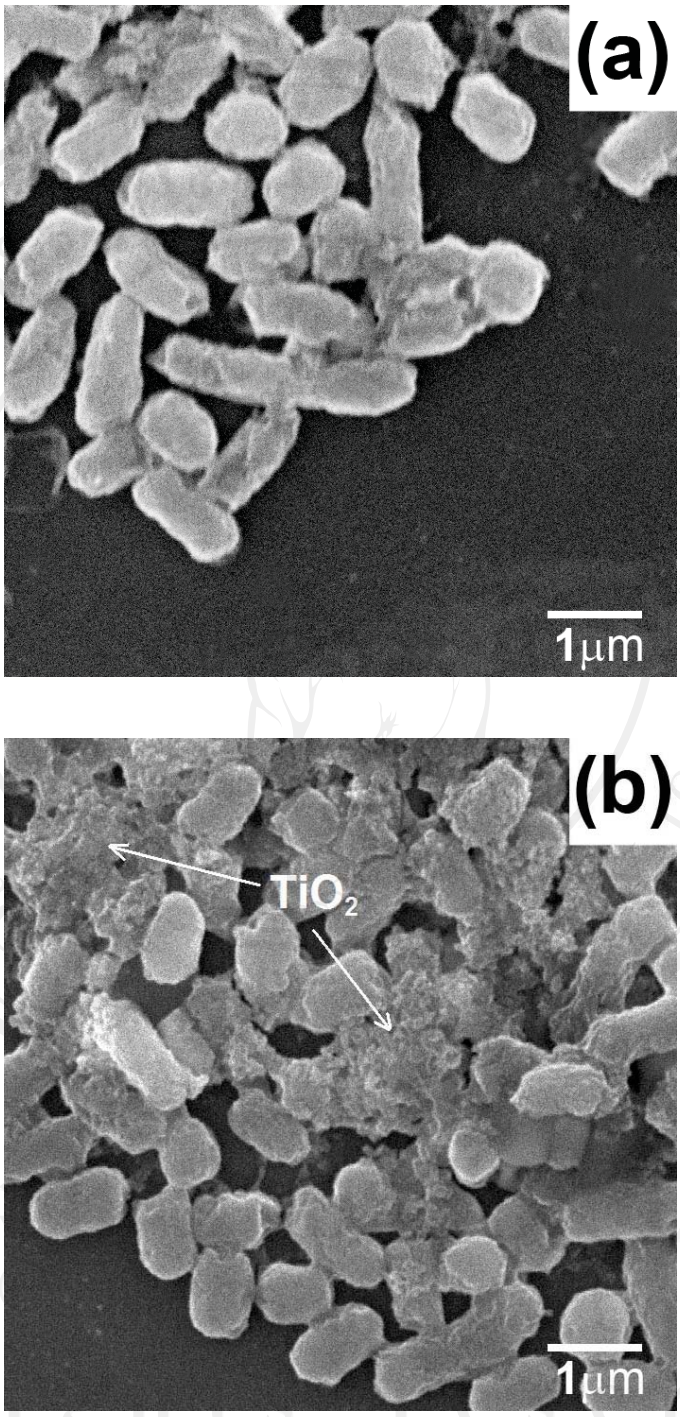

Figure 4.13 SEM images of (a) controlled and (b) treated *E.coli* cells with TiO_2 NPs under UV light for 4 h.

The results show that the structure of the treated cells was damaged due to the effect of photocatalytic reaction taking place on the surface of NPs which interact with the intact cells. The protection of the cell wall was deteriorated by an oxidative damage of the underlying cytoplasmic membrane. The reaction progressively increased the cell permeability, subsequently allowed the free efflux of intracellular contents and eventually leaded to the cell death [87,91].

An assumption of cell death from SEM was confirmed by TEM image (Figure 4.14),

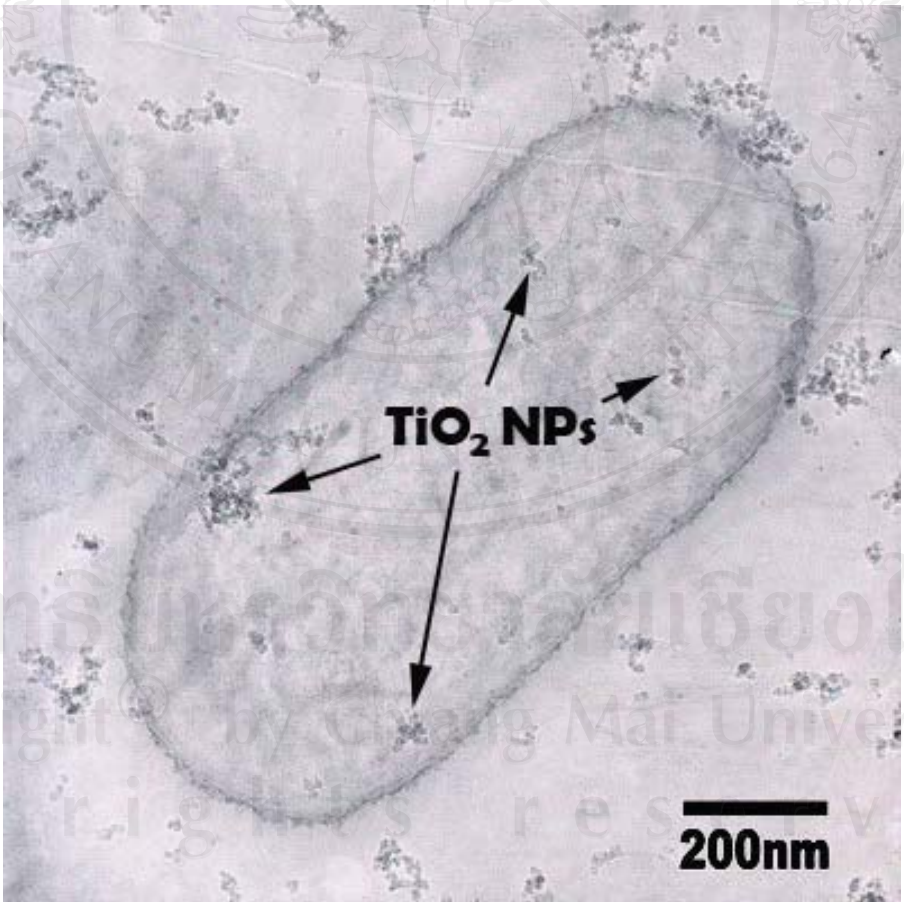

Figure 4.14 Cross section TEM image of treated *E.coli* cell with TiO_2 NPs under UV light for 4 h.

TiO_2 NPs migrated through the cell wall to the bacterial cell. It is clearly display that organelles inside the bacterial cell were burst, for example nucleoid region was disappeared when cell was treated with NPs. As a result, TiO_2 NPs can caused a direct attack of intracellular components and accelerated the cell death. Even in the dark condition, bacterial growth inhibition was also observed due to the additional mechanism. The corresponding results have been reported by mammalian cytotoxicity studies, where TiO_2 exerted oxidative stress in the dark under non-photocatalytic conditions [92-94].

4.2 Synthesis of Fe_2O_3 NPs by pyrosol method

This section presents the results of Fe_2O_3 NPs which successfully prepared by pyrosol technique. The effect of precursor concentration on the particle sizes and structural properties of the obtained particles are also discussed.

4.2.1 Morphology

Figure 4.15a shows the SEM images which clearly seen an individual Fe_2O_3 spherical particles. Experimentally determined value of the mean diameter for this sample is estimated to be about 850, 380 and 180 nm (see Figure 4.15b and Figure 4.16). From chapter 2 (page 39), Calculation of the theoretical mean diameter of Fe_2O_3 particles can be done by using the *Dd* value of Eq. (2.6) (the diameter of the misted droplet) and the constants into Eq. (2.7), as shown in Table 4.2. The theoretical mean diameter of Fe_2O_3 particles were about 1100, 565 and 265 nm with the precursor concentration of 1, 0.1 and 0.01 M, respectively (see Table 4.2 and Figure 4.16). Compared to the theoretical mean diameter, the relation of the particle size against the precursor concentration was similar direction which the sizes were decreased about two times with the decreasing of the precursor solution about ten times. According to the proportion of the particle sizes are related to the third root of the precursor concentration (Eq. 2.7).

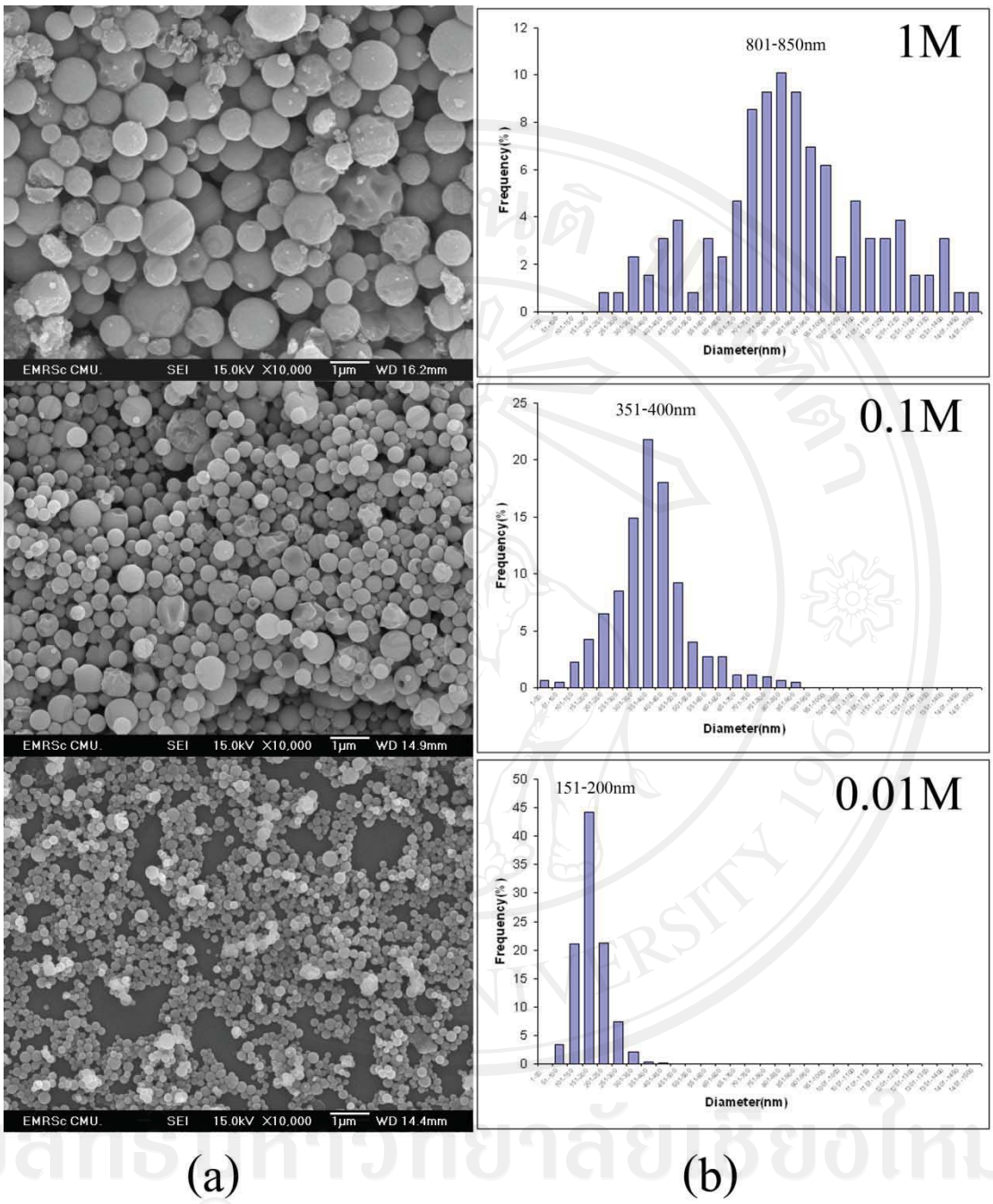

Figure 4.15 SEM images (a) and their size distribution of Fe_2O_3 NPs at the precursor concentrations of 0.01, 0.1 and 1 M.

Table 4.2 The calculated diameter of the misted droplets and mean particle size of α-Fe_2O_3 particles using Eqs. (2.6)* and (2.7)**

Concentration(M)	Solution density(kg/m^3)	*Dd* (μm)*	*TDp* (nm)**	*EDp* (nm)
1	1404	2.64	1101.27	851.25
0.1	1040.4	2.92	564.87	382.46
0.01	1004.04	2.95	265.32	182.25

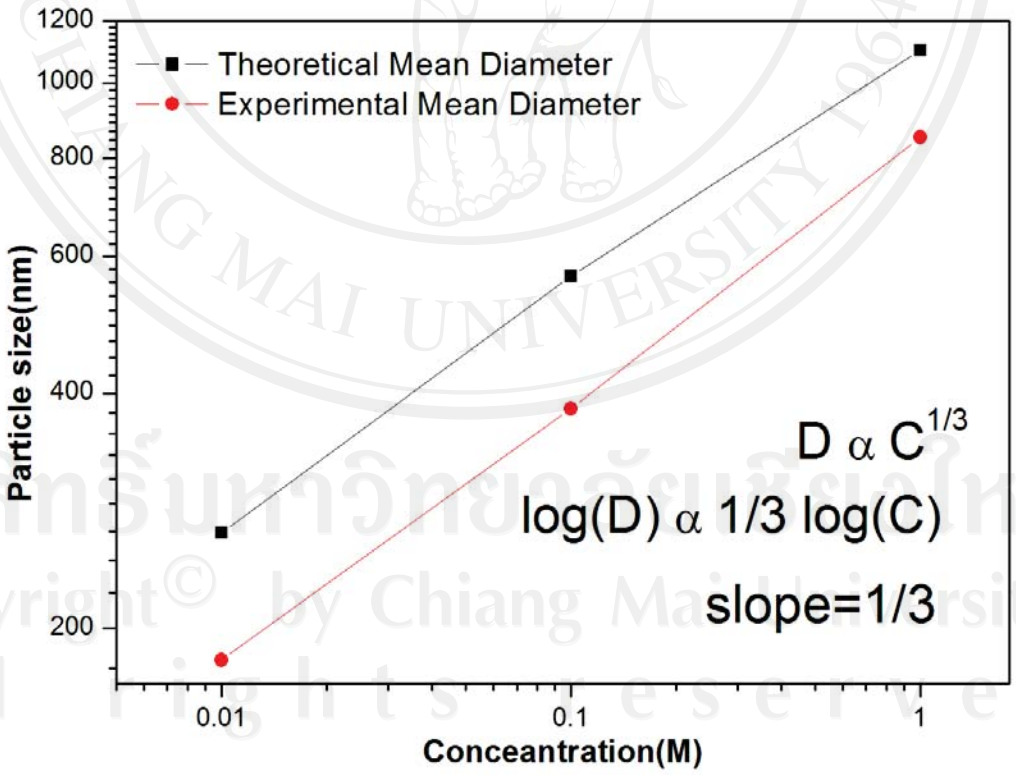

Figure 4.16 Plot of theoretical and Experimental mean diameter against various concentration of precursor solution.

4.2.2 Structural property

When the concentration of precursor solution varies from 1, 0.1 and 0.01 M but the temperature and flow rate are fixed and equal to 350°C and 340 ml/min, respectively. Structural of the deposited particles are characterized by XRD, as shown in Figure 4.17. XRD patterns indicate that the particles are almost α-Fe_2O_3 polycrystal phase (Hematite, JCPDF file 89-0599), which has structure with lattice parameters a=0.5032 nm and c=1.3733 nm. It is noted that the peak heights from the sample prepared with the 1 M condition are low. The poor crytallinity is probably originated by the large particle size. On the other hand, the samples obtained from the 0.1 and 0.01M conditions are better crystallized.

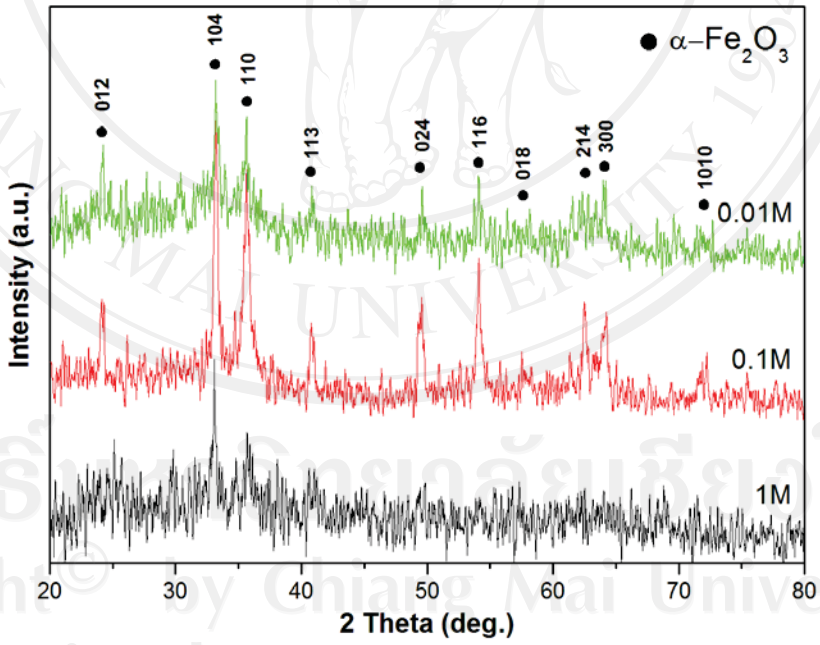

Figure 4.17 XRD patterns for α -Fe_2O_3 NPs with various concentration of precursor solution.

Raman spectrum of all samples (shown in Figure 4.18) exhibits seven strong vibrational peaks at about 218, 283, 397, 491, 598, 655 and 1291 cm^{-1}, corresponding to the typical frequencies observed for α-Fe_2O_3, although a small shift towards low wave-number is noted as compared to the bulk powders [95]. This result further confirmed the XRD analysis, indicating that the as-synthesized products were α-Fe_2O_3.

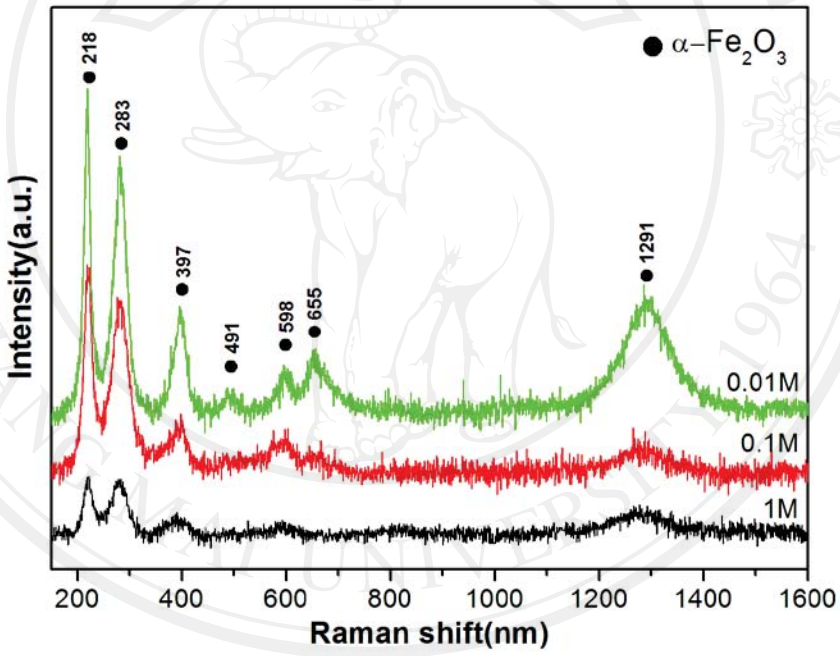

Figure 4.18 Raman spectrum of α -Fe_2O_3 NPs.